J. Electrochem. Sci. Eng. **16** (2026) 3099; https://doi.org/10.5599/jese.3099

Open Access : : ISSN 1847-9286

https://pub.iapchem.org/ojs/index.php/JESE

Original scientific paper

Effect of composition and crystal structure of CoRe alloys on electrocatalytic properties and hydrogen interaction

Yuliya Yapontseva[1,✉], Olena Ostapets[1], Oleksii Vyshnevskyi[2] and Valeriy Kublanovsky[1]

[1]*V. I. Vernadsky Institute of General and Inorganic Chemistry of the NAS of Ukraine, pr. Palladina 32/34, 03142 Kyiv, Ukraine*

[2]*M.P. Semenenko Institute of Geochemistry, Mineralogy and Ore Formation of the NAS of Ukraine, pr. Palladina 34, 03142 Kyiv, Ukraine*

Corresponding Author: ✉*juliya_yap@ukr.net*

Received: November 11, 2025; Accepted: February 08, 2026; Published: February 23, 2026

Abstract

This study investigates the codeposition of cobalt and rhenium from pyrophosphate-ammonia electrolytes. The results show that, depending on the deposition current density and the concentration of components in the solution, the coatings contain 17.7 to 43.8 at.% Re, with a high current efficiency reaching up to 76 %. The formation of a solid solution of rhenium in hexagonal close-packed (hcp) cobalt leads to an increase in lattice parameters and interplanar spacings along the (100), (101), and (110) planes compared to pure cobalt. CoRe alloys absorb a significant amount of hydrogen, which, during electrodeposition, promotes the formation of stressed coatings prone to cracking. During hydrogen evolution on the alloy surfaces in KOH solution, the expanded crystal lattice absorbs hydrogen atoms and facilitates hydride formation, which is characteristic of intermetallic compounds. The coatings that interact with hydrogen via both mechanisms (25 to 30 at.% Re) exhibit the highest electrocatalytic activity in the hydrogen evolution reaction. A further increase in rhenium content results in the formation of nano-crystalline textured coatings with a predominant (002) orientation, exhibiting lower electro-catalytic activity and reduced hydrogen absorption capacity.

Keywords

Cobalt, rhenium, electrolytic alloys, electrocatalysis; hydrogen evolution; absorption of hydrogen

Introduction

Rhenium, in its metallic form as well as in alloys with transition metals, oxides, sulphides, and selenides, serves as a promising component of electrocatalysts for the hydrogen evolution reaction (HER), offering a potential alternative to platinum-group metals in water electrolysis technologies. The review by Ramírez *et al*. [1] summarizes the most significant advances in rhenium-based electrocatalysts for HER, with a particular emphasis on acidic media. According to the Sabatier

principle [2], an ideal HER catalyst should interact with the adsorbed hydrogen intermediate (H*) neither too strongly nor too weakly. The interaction strength of H* with the catalyst surface and its correlation with catalytic activity plays a crucial role in the rational design of efficient hydrogen generation systems [3,4].

Compared to other refractory metals such as tungsten and molybdenum, rhenium is the only one that can be deposited individually from aqueous solutions. Rhenium coatings are obtained via electrochemical reduction of ReO_4^- ions from sulphate and sulphate-ammonium electrolytes [5,6]. In such electrolytes, the current efficiency for rhenium deposition is only 5-15 %. The stable thickness of the rhenium coating does not exceed 1.5 to 2.0 μm, since thicker coatings tend to crack and delaminate from the substrate. In air, especially in humid environments, rhenium readily oxidizes, changing colour to blue or dark blue due to the formation of a surface mixture of ReO_3 and ReO_2. To mitigate this instability, post-deposition thermal treatment in an inert atmosphere or vacuum is required. A fluoride-based electrolyte that enables deposition of rhenium coatings with a thickness of 3 to 5 μm, followed by mandatory annealing in an inert atmosphere, is proposed by Ivanova *et al*. [7].

The mechanism of rhenium electrodeposition from perrhenate ions is reviewed in detail by Eliaz and Gileadi [8]. The reduction pathway depends strongly on the pH of the solution, meaning that the reduction potential is largely determined by solution acidity. Additionally, concurrent hydrogen evolution often occurs, with some hydrogen atoms incorporating into the deposited metal. This alters the activity of rhenium in the surface layer and thus affects the equilibrium potential of the ReO_4^-/Re^0 electrode. In alkaline media, the overall reaction is presented by Equation (1):

$$ReO_4^- + 4H_2O + 7e^- \rightarrow Re + 8OH^- \quad (1)$$

The standard electrode potential of the ReO_4^-/Re^0 redox couple equals +0.363 V at pH 0 and -0.584 V at pH 14 *versus* the normal hydrogen electrode (NHE) [9,10]. The reduction of perrhenate ions most likely proceeds through a series of sequential steps, in which different oxides or hydroxides of rhenium form under equilibrium conditions depending on the solution pH. Several mechanisms for the electrodeposition of rhenium from aqueous solutions have been proposed [8,11,12]. These mechanisms include stepwise reduction of perrhenate ions to the metal *via* adsorbed hydrogen atoms and the formation of ReO_3 as an intermediate.

During the reduction of perrhenate, both direct electron transfer (with subsequent or simultaneous proton addition) and chemical reduction by atomic hydrogen are possible. Analysis of hydrogen evolution on rhenium surfaces highlights the importance of accounting for hydrogen surface coverage and concentration polarization of molecular hydrogen [13]. At low overpotentials, due to the high hydrogen adsorption energy on rhenium (6.9 kJ mol^{-1}), electrochemical desorption is the rate-limiting step. As the overpotential increases, the overall rate becomes controlled by the slower discharge of protons, which depends on the degree of hydrogen surface coverage. The strong hydrogen sorption capacity of rhenium and the inhibition of hydrogen evolution at the desorption stage suggest that perrhenate reduction via adsorbed hydrogen is feasible. However, the possibility of reduction via direct electron and proton transfer cannot be excluded.

The mechanism of thin rhenium film formation on electrode surfaces has been studied using in-situ ellipsometry by Zerbino and Castro Luna [14]. It is shown that on gold substrates, rhenium deposits as a monolayer concurrently with molecular hydrogen evolution. In contrast, on platinum, rhenium monolayer formation occurs within the potential region corresponding to adsorbed hydrogen formation.

Based on the aforementioned concepts of the rhenium deposition mechanism, the metal is expected to form on the cathode in a highly dispersed and stressed state. This results from intense

hydrogenation and the reduction of rhenium from hydroxide films, which may be incorporated into the cathodic deposit.

Rhenium forms electrolytic alloys with iron-group metals [8,15,16], with the rhenium content varying across a wide range up to 93 at.%, which distinguishes rhenium alloys from those of other refractory metals. From alkaline citrate, pyrophosphate, and polyligand electrolytes, rhenium does not deposit individually but only co-deposits with iron-group metals to form an alloy in our case, with cobalt.

In our previous study [17], we demonstrated that the chemical composition of the alloy strongly depends on the kinetics of cobalt electroreduction, which is determined by the composition of the electrochemically active cobalt complex and the overpotential of its discharge. When cobalt reduction is hindered, as in alkaline citrate electrolytes containing the complex $[CoCit_2]^{4-}$, the resulting deposit contains a high rhenium content, reaching up to 78 at.%. Conversely, when cobalt is reduced at low overpotential and with high current efficiency, as in the case of the polyligand citrate-pyrophosphate complex [Co(Cit)(PPi)], the rhenium content in the resulting alloy is significantly lower, not exceeding 23 at.%.

In the present work, we investigate the electrodeposition and properties of CoRe alloys obtained from a polyligand electrolyte containing both pyrophosphate ions and ammonia. The kinetics of cobalt reduction from a pyrophosphate-ammonia electrolyte has been examined in our previous study [18], where we showed that cobalt from a polyligand complex is reduced at lower polarization and with lower current efficiency compared to that from a pure pyrophosphate electrolyte. While this would be a disadvantage for cobalt-only deposition, in the context of rhenium alloy deposition it becomes an advantage, as the reduction of perrhenate ions proceeds via surface-mediated reactions involving adsorbed hydrogen. As discussed earlier, this reduction pathway depends on the degree of hydrogen coverage on the cathode surface.

Experimental

Materials and synthesis

The electrodeposition of CoRe alloys is carried out from pyrophosphate-ammonia electrolytes with the following composition 0.1 mol L^{-1} $CoSO_4$, 0.01 to 0.05 mol L^{-1} $KReO_4$, 0.5 mol L^{-1} $K_4P_2O_7$ and 0.3 mol L^{-1} $(NH_4)_2CO_3$. The experiments are conducted under natural convection in a thermostated cell at 50 °C in galvanostatic mode using a LIPS-35 (“KyivPrylad”, Ukraine) direct current power supply. For obtaining stationary voltammetric curves of metal codeposition into the alloy, a copper end-face disk electrode (5 mm in diameter) sealed in Teflon was used. For the electrodeposition of coatings and subsequent characterization of their composition, structure, and properties, copper plates with an area of 1 cm^2 were used, and a platinum plate is used as the anode. The pH of the electrolyte is maintained at 9.0.

Scanning electron microscope and energy-dispersive X-ray spectroscopy

The morphology and chemical composition of samples were studied by using a JSM-6700F field emission scanning electron microscope equipped with a JED-2300 energy-dispersive spectrometer (JEOL, Japan). The operating conditions were as follows: 20 kV accelerating voltage, 0.75 nA beam current, 1 µm beam size. The counting time for energy-dispersive X-ray spectroscopy (EDS) analyses was 60 s. Pure Co and Re were used as standards. The raw counts (Co, Kα; Re, Lα) were corrected for matrix effects with a ZAF algorithm implemented by JEOL. Three to five spots per each sample were analysed.

X-ray phase analysis

The X-ray patterns were recorded on a diffractometer (DRON-4) in Bragg - Brentano geometry with Mo-K_α radiation which operates at 45 kV and 20 mA in 0.05 degree-steps with 4 s exposure at point.

X-ray photoelectron spectra of CoRe alloy

The studies of Co-Re alloy samples were carried out using a modernized ES-240UM X-ray photoelectron spectrometer (XPS). Calibration of the spectrometer was performed at the beginning, middle, and end of the energy scale using gold and copper standards by recording the maxima of the Cu $2p_{3/2}$, Cu 3p, Au $4f_{7/2}$, and Au $4d_{5/2}$ lines. The obtained binding energies were: *E* (Au $4f_{7/2}$) = 84.0 eV, *E* (Cu 3p) = 75.1 eV, E (Au $4d_{5/2}$) = 335.2 eV and *E* (Cu $2p_{3/2}$) = 932.6 eV, which correspond to the standard values accepted for these lines [19].

The spectrometer was equipped with an X-ray gun with a magnesium anode ($E_{MgK\alpha}$ = 1253.6 eV, *P* = 300 W). The working vacuum in the spectrometer chamber was 30 MPa. The absolute resolution measured for the Au $4f_{7/2}$ peak was 1.0 eV. The obtained spectra of the Re 4f and Co $2p_{3/2}$ core levels were deconvoluted into components, with the position (*E*) and intensity (*I*) of the components used as variable parameters.

Kinetic studies of metal codeposition into alloys

The co-deposition of cobalt and rhenium into an alloy is investigated using steady-state voltammetry (1 mV s^{-1}) and linear sweep voltammetry with potential scan rates ranging from 5 to 100 mV s^{-1}. Measurements were performed in a thermostated three-electrode electrochemical cell using an Ag/AgCl reference electrode in 3 M KCl and an MTech PGP-550S potentiostat. The experiments were conducted at 50 °C for solutions containing 0.01 mol L^{-1} potassium perrhenate, and at 60 °C for solutions containing 0.05 mol L^{-1} $KReO_4$, due to the limited solubility of perrhenate in the electrolyte at lower temperatures. The separation of the partial metal deposition curves is based on the current efficiency of each metal, which is determined using Faraday's law and the weight gain of the electrode after deposition.

According to Faraday's law, the cathodic current efficiency (CE) of metals and alloys is expressed by Equation (2), taking into account the weight gain of the sample after electrodeposition:

$$CE_{alloy} = CE_{Re} + CE_{Co} = \frac{mw_{Re}}{k_{Re} i \tau} + \frac{mw_{Co}}{k_{Co} i \tau} \quad (2)$$

where *m* / g is the weight gain of the sample after electrodeposition, *w* / wt.% is the content of the element, *k* / g A^{-1} h^{-1} is the electrochemical equivalent of the elements, *i* / A is the current, and τ / h is the electrolysis time.

Kinetic studies of hydrogen evolution and absorption

The kinetics of hydrogen evolution on CoRe alloys is investigated using steady-state voltammetry (1 mV s^{-1}) in 1 M KOH solution at 25 °C. The dependence of the amount of absorbed hydrogen on the cathodic exposure time at a current density of 40 mA cm^{-2} is studied by means of linear sweep voltammetry (LSV) at different sweep rates (10 to 100 mV s^{-1}) and chronopotentiometry (at an anodic current density of 1.2 mA cm^{-2}). The amount of hydrogen absorbed is determined by calculating the area under the anodic and cathodic peaks in the voltammetric curves.

The amount of electric charge consumed during hydrogen oxidation was calculated from the area under the voltammetric peak. The peak area was determined using the trapezoidal method. The amount of electric charge was calculated considering the potential sweep rate according to Equation (3):

$$Q = S_p / \nu \quad (3)$$

where Q / Ah is the amount of electric charge, S_p / V A is the geometric area under the peak and ν / V h^{-1} is the potential sweep rate.

Results and discussion

Electrodeposition of alloys

As shown in Figure 1(a), in the current density range of 5 to 20 mA cm^{-2} and at a ReO_4^- concentration of 0.01 mol L^{-1}, the coatings contain approximately 26 at.% rhenium. With further increases in current density, the rhenium content decreases to 17.7 at.%, which is somewhat higher than the values obtained at the same perrhenate concentration in polyligand citrate-pyrophosphate electrolytes (12 to 23 at.% Re) [17]. When the concentration of perrhenate ions in the solution is increased to 0.05 mol L^{-1}, the rhenium content in the coatings rises to 30.0 to 43.8 at.%. A distinct maximum is observed at a deposition current density of 10 mA cm^{-2}, the origin of which is discussed below.

Figure 1(b) shows that rhenium accounts for most of the overall current efficiency. The current efficiency of the alloy remains relatively high compared with other refractory metals, but it decreases with increasing deposition current density. The coating thickness was 5 to 10 µm, depending on the current density. The electrolysis time was 1 hour.

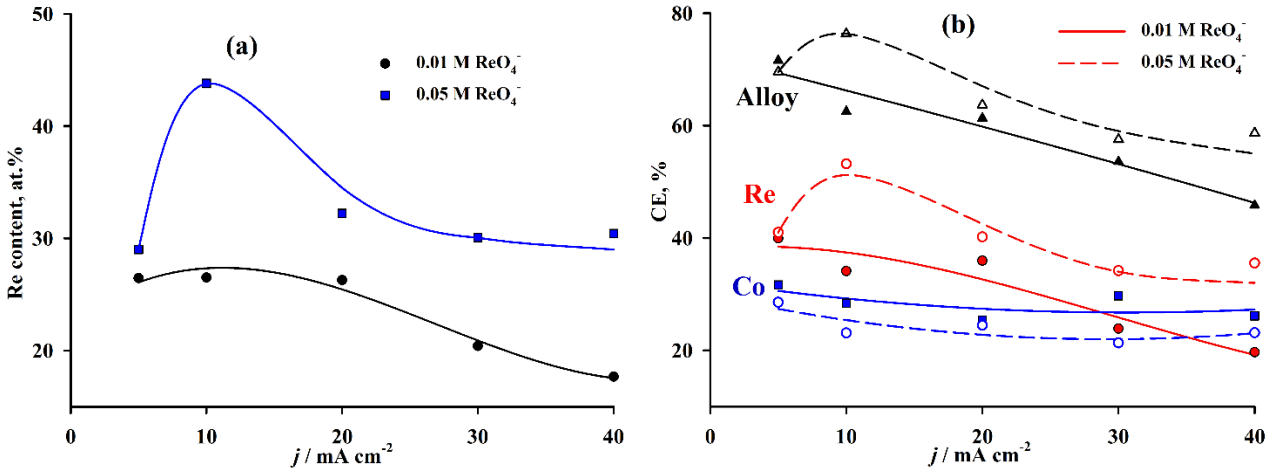

Figure 1. *Dependence of: (a) rhenium content in the CoRe alloys and (b) current efficiency of the individual metals and the CoRe alloy on the deposition current density. Alloys were deposited from 0.01 and 0.05 M ReO_4^-*

CoRe alloys deposited from the pyrophosphate-ammonia electrolyte form smooth and shiny coatings. Here, however, as shown in Figure 2, in correlation with the chemical composition data, an increase in rhenium content leads to the formation of stressed coatings and crack formation.

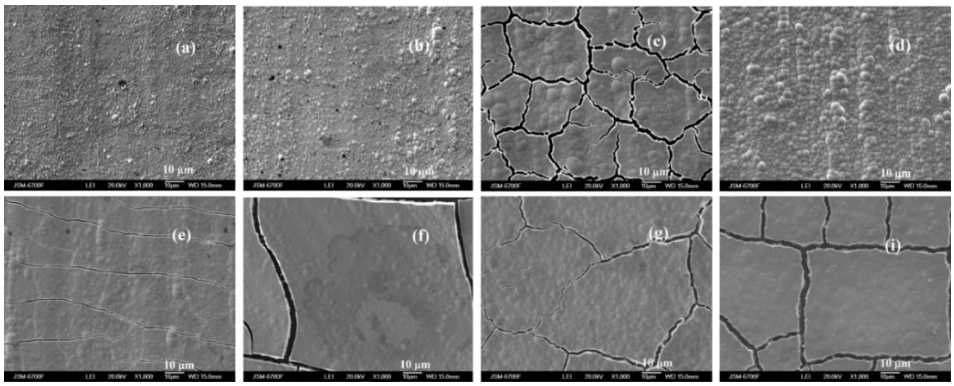

Figure 2. *Surface micrographs of the CoRe alloys as a function of electrolyte composition and deposition current density: (a) to (d) solution with 0.01 M ReO_4^-; (e) to (i) solution with 0.05M ReO_4^- at: (a) and (e) 5; (b) and (f) 10; (c) and (g) 20; (d) and (i) 40 mA cm^{-2}*

Since rhenium and cobalt exhibit unlimited mutual solubility with the formation of equilibrium solid solutions, this behaviour of electrodeposited coatings is attributed to the incorporation of impurities, in this case, hydrogen atoms generated at the electrode surface.

Figure 3 shows that alloy deposition occurs within the limiting-current region of metal reduction and intense hydrogen evolution. Hydrogen bubbles contribute to the mixing of the near-electrode layer, resulting in a smoothed and poorly defined limiting current plateau on the experimental voltammetric curve. This effect is especially pronounced in the solution containing 0.05 mol L^{-1} perrhenate ions, from which the most stressed coatings with the highest rhenium content are deposited.

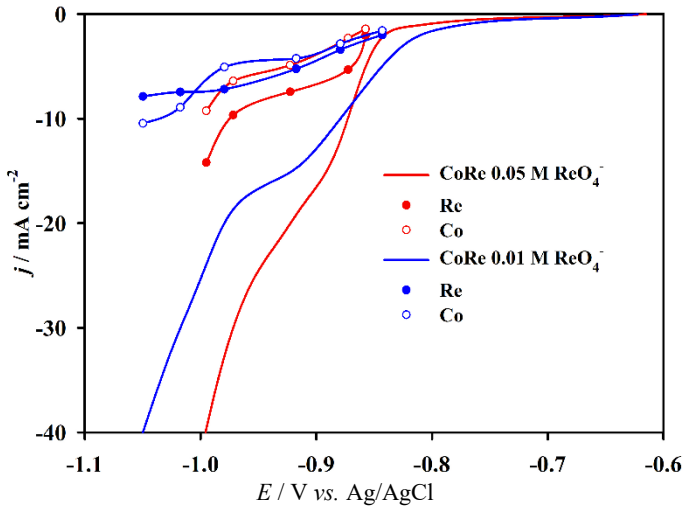

Figure 3. *Experimental linear sweep steady-state voltammograms of CoRe alloys deposition and partial deposition curves of the individual metals*

An increase in the perrhenate ion concentration in the solution shifts the onset potential for alloy deposition to more negative values by approximately 30 mV, and the limiting current plateau is reached earlier. Figure 3 presents the partial deposition curves for the individual metals in the alloy, constructed from the current efficiency data for each element. It is evident that at low current densities, *i.e*. within the kinetic control region, the partial deposition currents of both metals are equal. In the solution with a lower concentration of perrhenate ions (0.01 mol L^{-1}), two limiting current regions are observed for cobalt: 4.5 mA cm^{-2} in the potential range of -0.90 to -0.98 V and 10.3 mA cm^{-2} at potentials more negative than -1.02 V. The limiting current for rhenium ions (7.5 mA cm^{-2}) is reached at more negative potentials (around -0.97 V), within the region of intensive gas evolution, where no distinct inflection points are visible on the polarization curve. For the solution containing 0.05 mol L^{-1} perrhenate ions, it is evident that two limiting current plateaus should also be present. However, the second one is not reached under the experimental conditions due to the limitation of the maximum applicable current density. The current density is limited in this case due to reduced coating quality and a significant decrease in overall current efficiency. The observed limiting current for cobalt was 5.3 mA cm^{-2} in the potential range of -0.90 to -0.97 V, and for rhenium, 7.4 mA cm^{-2} in the range of -0.87 to -0.97 V.

The partial current of cobalt deposition increases synchronously with that of rhenium, even though the cobalt ion concentration is high and constant in both solutions. This behaviour may indicate that cobalt is deposited exclusively as an alloy. At a current density of 10 mA cm^{-2}, the first limiting current is observed, and, under these conditions, the maximum rhenium content in the alloy is achieved.

The nature of the limiting currents is investigated using linear sweep voltammetry at different sweep rates. As shown in Figure 4, increasing the potential scan rate results in higher limiting

currents and shifts the potential at which they are reached toward more negative values. Figure 4 shows that all linear voltammograms at scan rates of 5 to 100 mV s^{-1} exhibit two limiting-current plateaus. These limiting currents do not have clearly defined peaks but are smooth plateaus due to the intense hydrogen evolution at the cathode, which promotes mixing of the near-electrode layer and changes the rate of delivery of reacting species to the cathode.

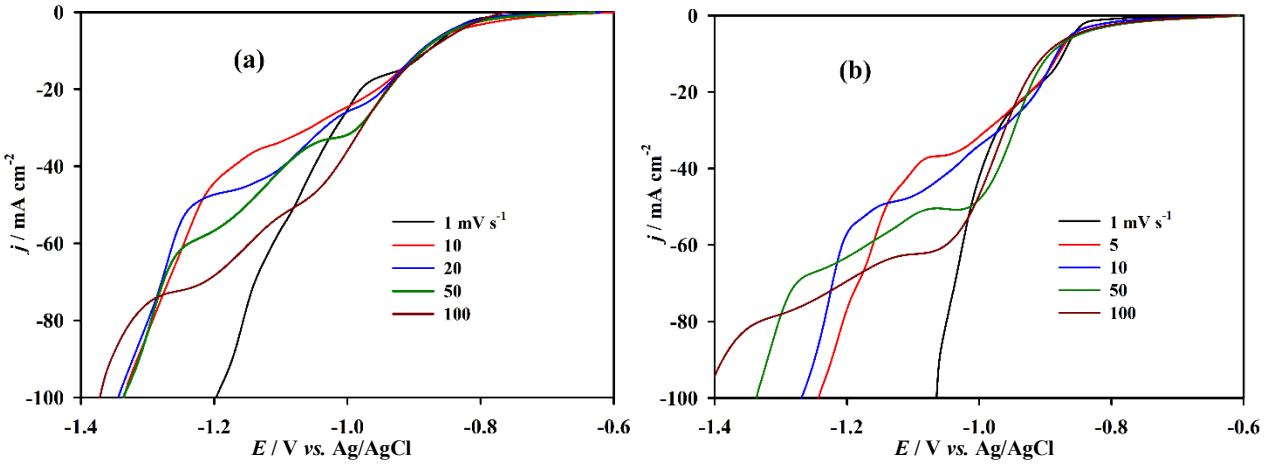

Figure 4. *(a) linear sweep voltammograms of alloy deposition from electrolytes containing 0.01 mol L^{-1} ReO_4^- and (b) 0.05 mol L^{-1} ReO_4^- at different potential scan rates, as indicated in the figure*

The rate-limiting stage was determined using the Semerano criterion (X_s) [20]. The dependencies of peak current (j_p) versus potential sweep rate (ν) plotted in j_p - $\nu^{1/2}$ coordinates in Figure 5(a) are linear but do not pass through the origin.

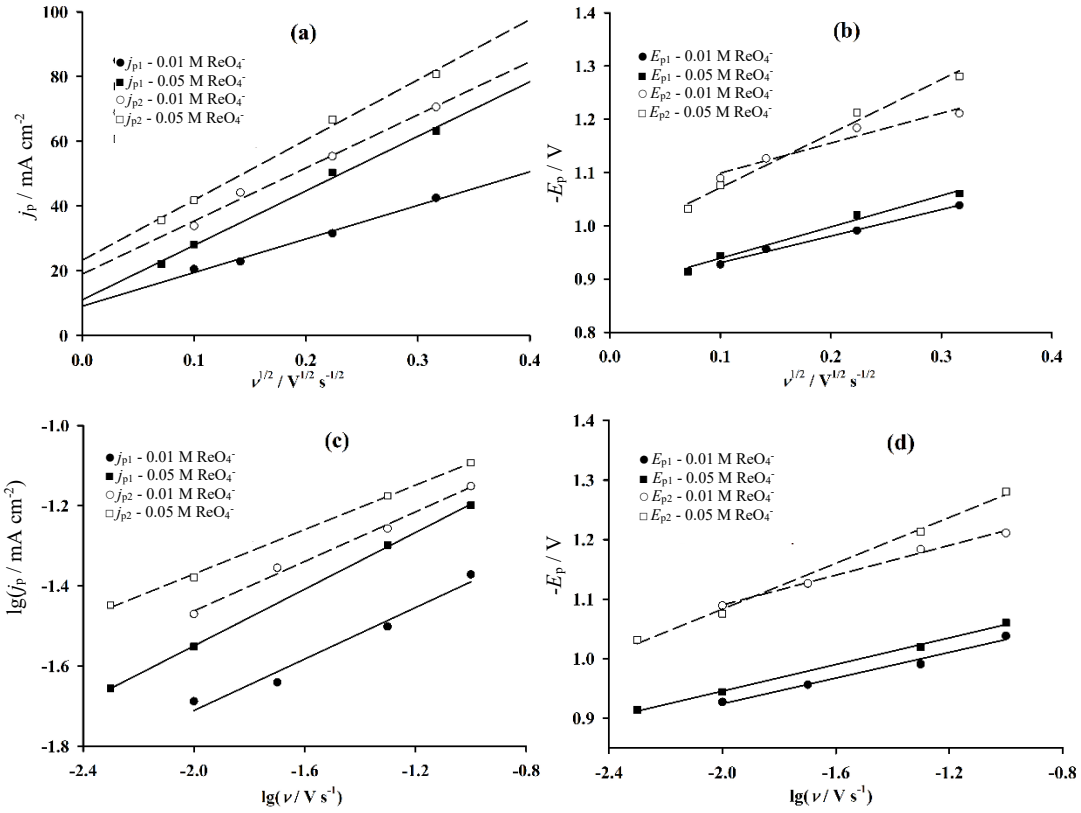

Figure 5. *Dependence of: (a) peak current density and (b) peak potential on the square root of potential scan rate, (c) log current density and (d) peak potential on log potential scan rate for CoRe alloys deposited from 0.01 and 0.05 M solutions of ReO_4^-, where j_{p1}, j_{p2} and E_{p1}, E_{p2} are the current and potential of the first and second peaks, respectively*

The Semerano criterion, calculated based on the slope of the dependence of the first and second peak currents on the potential scan rate in log j_p - log ν coordinates shown in Figure 5(c), is in the range of Semerano criterion X_s = 0.28 to 0.35. The effective transfer coefficient (α'), calculated from the slope of E_p - log ν straight line [21] (Equation (4)) shown in Figure 5(d), lies in the range of α' = 0.31 to 0.53.

$$\alpha' = \frac{2.3RT}{F \text{ tg } \beta} \tag{4}$$

where tg(β) is the slope of the dependence E_p *vs.* log ν.

These calculated criteria (X_s) indicate that alloy deposition proceeds under mixed diffusion-kinetic control, involving a two-step electron-transfer process. The fact that the linear plots in j_p - $\nu^{1/2}$ coordinates do not intersect the origin may suggest the occurrence of a preceding chemical dissociation step of the polyligand complexes $[Co(NH_3)_2(P_2O_7)]^{2-}$, followed by their electrochemical reduction, as previously discussed in [18].

Crystal structure of CoRe alloys

Figure 6 presents the XRD patterns of CoRe alloys deposited at current densities of 10 and 40 mA cm^{-2}, corresponding to the maximum and minimum rhenium content in the coatings for each of the studied electrolytes, as shown in Figure 1a.

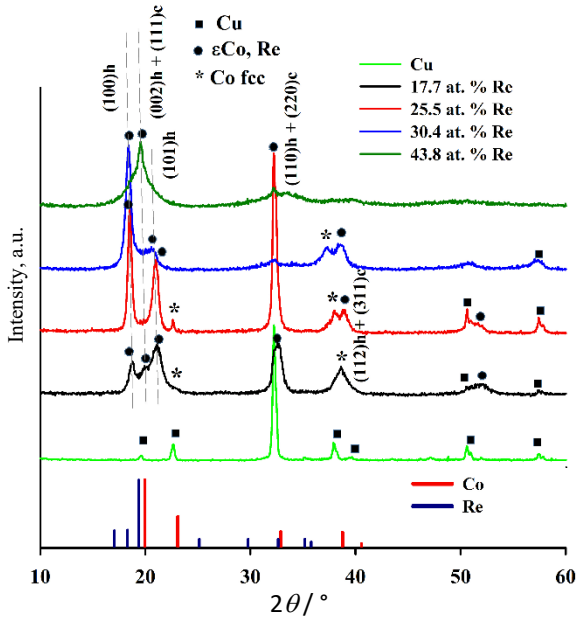

Figure 6. *XRD patterns of CoRe alloys as a function of rhenium content in the coatings*

The diffraction pattern of the copper substrate onto which the coatings are deposited is also included in the figure.

It is well known that cobalt exists in two allotropic modifications: α-Co with a hexagonal close-packed (hcp) structure and β-Co with a face-centered cubic (fcc) structure, with the phase transition temperature between α ↔ β being 427 °C. The internal structure of cobalt changes from the densely packed hcp form below this critical temperature to the fcc structure at higher temperatures [22]. Both cobalt modifications, which differ in their physicochemical and mechanical properties, can coexist in electrodeposited coatings [23]. According to Ma *et al*. [24], low pH and low overpotentials during electrodeposition favour the formation of the thermodynamically stable fcc phase, while high pH and high overpotentials promote the formation of the metastable hcp phase.

In our case, for the coating containing the lowest amount of rhenium (17.7 at.%), overlapping diffraction peaks are observed that correspond to hcp cobalt and can be assigned to the (100), (002), and (101) planes, as well as (110) and (112) reflections partially superimposed with the peaks of the copper substrate. The 2θ values are slightly shifted toward lower angles compared to pure cobalt [25]. A minor amount of cobalt with an fcc structure is also present in the coating [26]. Peak separation and lattice parameter calculations are performed using Origin 10.0 software.

As the rhenium content in the coating increases to 25.5 at.%, an increase in the intensity of the diffraction peaks (100), (101), and (110) is observed, along with the separation of the (112) cobalt hcp and (311) fcc peaks, and a significant decrease in the intensity of the (002) maximum. A further increase in rhenium content leads to broadening of all observable peaks, and at the maximum content achieved under the experimental conditions, 43.8 at.% Re a nanocrystalline textured coating with basal planes (001) parallel to the coating surface.

For all obtained diffraction patterns, diffraction angle shifts, lattice parameters *a* and *c*, crystallite sizes, and interplanar spacings in CoRe alloys were calculated as functions of rhenium content. According to the Scherrer equation, the crystallite size can be estimated by Equation (5):

$$D = \frac{K\lambda}{\beta_{hkl}\cos\theta} \quad (5)$$

where θ is the diffraction angle; λ is the X-ray wavelength (λ_{Mo} = 0.07093187 nm); β_{hkl} is the full width at half maximum (FWHM) of the peak; *D* is the crystallite size.

The obtained results are presented in Figure 7.

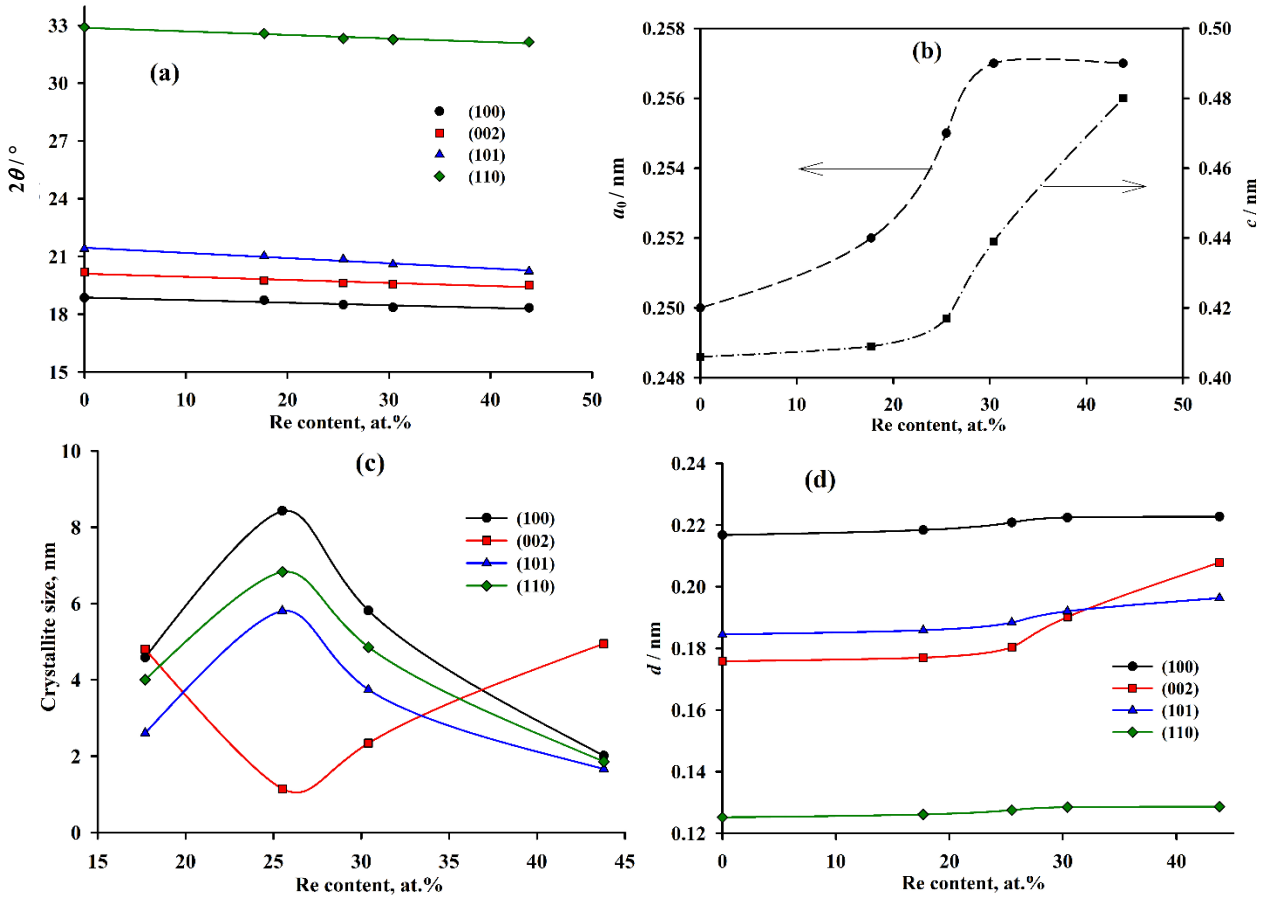

Figure 7. *Dependence of diffraction angle (a), hcp lattice parameters (b), crystallite size (c), and interplanar spacing (d) on the rhenium content in the CoRe coating*

The shift in the 2θ angle toward lower values (Figure 7a) indicates an expansion of the crystal lattice due to the formation of a solid solution of rhenium in cobalt. Cobalt and rhenium form a continuous series of solid solutions, as shown in the phase diagram reported by Barabash and Koval [27]. The *c*/*a* ratio changes only slightly from pure cobalt to the alloy containing 25.5 at.% Re (1.6220-1.6337) but increases significantly to 1.7092 and 1.8662 for alloys with 30.4 and 43.8 at.% Re, respectively, which is attributed to the incorporation of a metal with a larger atomic radius. This lattice expansion also increases interplanar spacing (Figure 7d). It is noteworthy that the most pronounced changes in interplanar spacing occur for the (002) planes when the rhenium content in the coating exceeds 30.4 at.%. All electrodeposited CoRe alloys obtained from pyrophosphate-ammonia electrolytes exhibit a nanocrystalline structure. The maximum crystallite size does not exceed 8 nm in the coating containing 25.5 at.% Re (Figure 7(c)). However, for the (002) plane, an opposite trend is observed: the largest crystallite size corresponds to conditions in which the (002) orientation becomes dominant. According to Vicenzo and Cavallotti [28], the appearance of the (002) hcp + (111) fcc reflection indicates a destabilizing effect of hydrogen evolution on the mixed structure, which tends to accommodate the densest crystallographic planes perpendicular to the surface.

Rhenium's unique ability to form numerous binary σ- and χ-phases makes it a key element in the understanding and design of alloys, particularly those containing refractory metals [29]. Furthermore, according to [30-32], rhenium and cobalt can form intermetallic phases of compositions CoRe and $Co_{0.8}Re_{0.2}$. Although pure rhenium does not form hydrides, rhenium-containing alloys, including electrodeposited ones [33], are capable of absorbing significant amounts of hydrogen, which will be discussed in the following section.

X-ray photoelectron spectra of CoRe alloy

The valence states of the elements on the surface of the CoRe alloy coating containing 17.7 at.% Re was investigated by XPS.

Figure 8a shows the deconvoluted Re $4f_{7/2}$ spectrum of rhenium atoms in the CoRe alloy. The main component with a binding energy of *E* (Re $4f_{7/2}$) = 40.5 eV corresponds to metallic rhenium (Re^0). In the region of *E* (Re $4f_{7/2}$) = 41.7 eV, a signal corresponding to rhenium dioxide (ReO_2) was detected. The component with *E*(Re $4f_{7/2}$) = 44.8 eV corresponds to rhenium trioxide (ReO_3), while the component at *E* (Re $4f_{7/2}$) = 43.4 eV is associated with the presence of perrhenate species (ReO_4^-) [34,35]. In Figure 8b, the deconvoluted Co $2p_{3/2}$ spectrum of cobalt atoms in the CoRe alloy is presented.

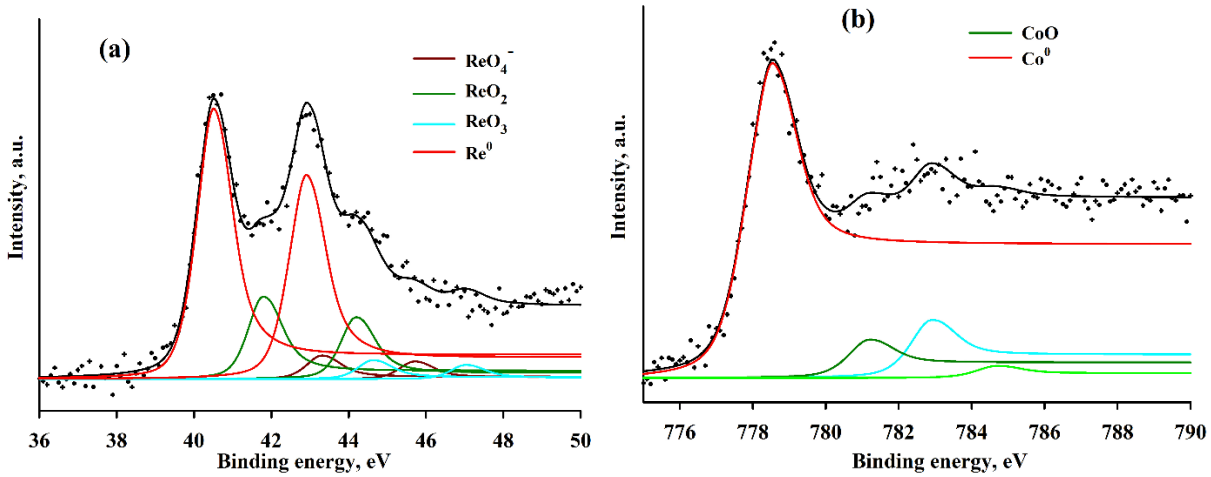

Figure 8. *Deconvoluted Re$4f_{7/2}$ spectrum of rhenium atoms (a) and Co $2p_{3/2}$ spectrum of cobalt atoms (b) in the CoRe alloy containing 17.7 at.% of rhenium*

The main component with a binding energy of *E* (Co $2p_{3/2}$) = 778.5 eV corresponds to metallic cobalt atoms. The signal in the region of *E* (Co $2p_{3/2}$) = 781.3 eV may be associated with the CoO phase. The contributions to the spectrum in the regions of *E* (Co $2p_{3/2}$) ≈ 783.0 and 784.7 eV are satellites [36,37].

The spectra were deconvoluted into individual components, and the integral area of each was determined after subtraction of the nonlinear background (Table 1).

Table 1. *Binding energy of the phases and their content in the coating*

Rhenium containing phases	
E (Re $4f_{7/2}$) / eV (J)	Content, %
40.5 (6.5×10^{-18})	69.6
41.7 (6.7×10^{-18})	20.1
43.4 (6.9×10^{-18})	5.8
44.8 (7.2×10^{-18})	4.5
Cobalt containing phases	
E (Co $2p_{3/2}$) / eV (J)	Content, %
778.5 (1.24×10^{-16})	89.5
781.3 (1.25×10^{-16})	10.5

The presence of oxide compounds on the surface of rhenium-containing alloys is typical. Oxide forms arise due to incomplete reduction of Re(VII) *via* electrochemical and catalytic mechanisms [35], as well as due to interaction with atmospheric oxygen during storage. The authors of [38] also reported the presence of nonstoichiometric oxides and a mixture of various rhenium oxide forms on the surface of electrolytic Ni-Re alloys deposited from a sulfamate-citrate electrolyte, which is likewise confirmed by our experimental results.

Electrocatalytic performance of CoRe alloys and their interaction with hydrogen

The electrocatalytic activity of the alloys in the hydrogen evolution reaction, as well as hydrogen absorption and desorption during electrolysis, is investigated in 1 M KOH solution. As shown in Figure 9, the hydrogen evolution overpotential decreases on CoRe alloys containing 17.7-30.4 at.% rhenium. ΔE in Figure 9 is polarization calculated relative to the equilibrium potential of the hydrogen reaction in this solution.

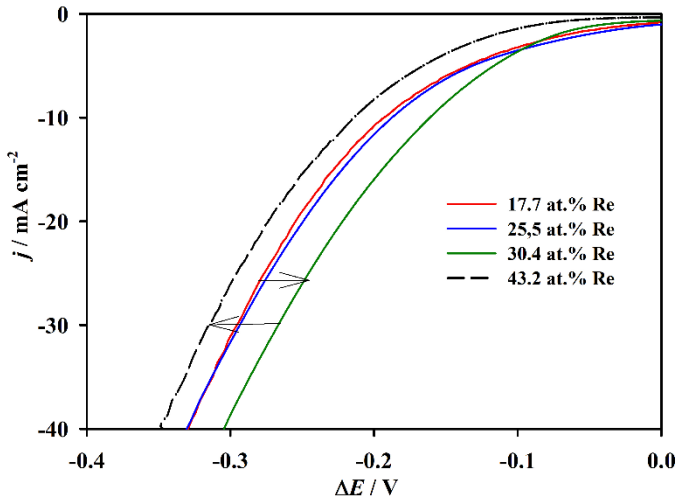

Figure 9. *Steady-state linear sweep voltammograms of hydrogen evolution on CoRe alloys with varying rhenium content in 1.0 M KOH*

Further increase in rhenium content leads to a noticeable inhibition of the reaction, consistent with previously reported data on the properties of Re-rich alloys [17,39,40]. The exchange current density for hydrogen evolution on the obtained alloys ranges from j_0 = 0.39 to 1.00 mA cm^{-2}, indicating that these alloys are effective electrocatalysts for the hydrogen evolution reaction (HER). It is important to note that in a KOH solution, hydrogen evolution is the target reaction, whereas during alloy electrodeposition, it is a parasitic and undesirable process. Nevertheless, HER electrocatalysis manifests itself in both cases: during coating deposition, it not only decreases the current efficiency of alloy formation but also induces internal stresses and cracking due to hydrogen absorption.

Hydrogen electroadsorption on CoRe alloys plays a crucial role in evaluating the influence of parallel HER during electrodeposition and in the intentional electrocatalytic production of hydrogen [41]. Since refractory metal alloys of the iron subgroup can only be deposited within the hydrogen evolution region, several physicochemical properties of the deposits, including their electrocatalytic activity, inherently depend on the amount and state of adsorbed or absorbed hydrogen. Among alloys of refractory metals (such as those containing tungsten, molybdenum, and rhenium) Re-based alloys demonstrate a distinctive feature: rhenium exhibits intrinsically low hydrogen overpotential, leading to greater hydrogen adsorption, as previously shown for NiRe alloys [42].

Key factors influencing hydrogen absorption include the following: (a) the discharge mechanism must involve metal-hydrogen (M-H) bonding; therefore, acidic solutions are particularly susceptible to hydrogen uptake; (b) hydride formation is possible, and such hydrides may exhibit ionic, covalent, or metallic bonding; (c) mechanical occlusion of hydrogen may occur at grain boundaries, pores, or voids, which may represent a physical rather than a chemical mechanism; (d) metals such as Pd and Re inherently have low hydrogen overpotentials and can absorb large amounts of hydrogen.

The ability of CoRe alloys to absorb significant amounts of hydrogen is investigated by voltammetric analysis in KOH solution under various exposure times during intense hydrogen evolution. First, we consider the behaviour of the alloy containing the minimum rhenium content under the experimental conditions 17.7 at.%. Figure 10a shows the steady-state cyclic voltammogram (1 mV s^{-1}) of hydrogen evolution on a CoRe alloy containing 17.7 at.% Re. In the potential range from -1.05 to -0.62 V, an anodic current is observed.

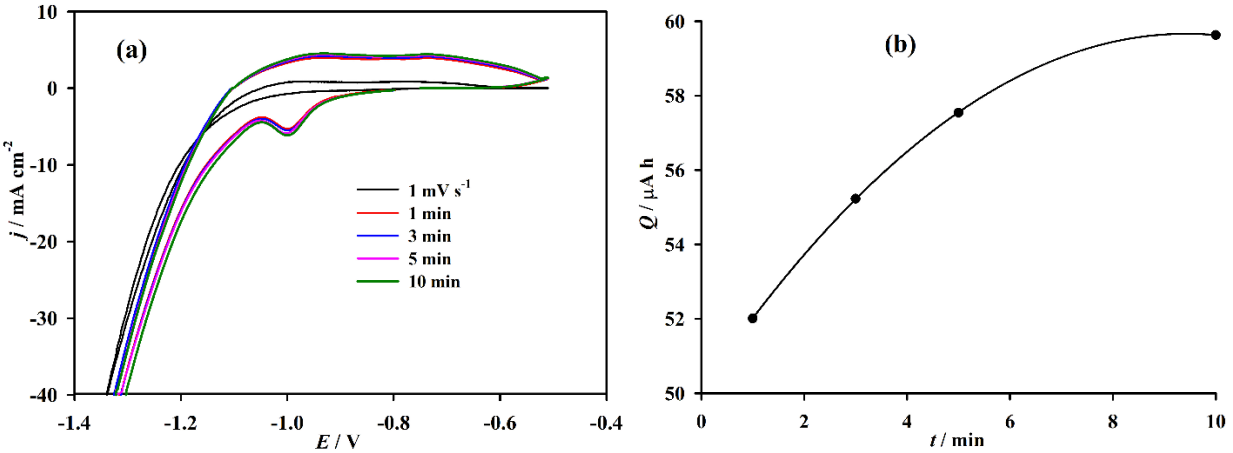

Figure 10. *(a) Cyclic voltammograms of hydrogen oxidation/reduction and (b) the amount of charge, associated with hydrogen oxidation at CoRe alloy (17.7 at.% Re) in 1.0M KOH, as a function of hydrogen evolution time (1 to 10 min) at 40 mA cm^{-2}*

To determine the nature of this current, a series of voltammograms is recorded at a scan rate of 10 mV s^{-1} using the following procedure: starting from the open circuit potential (-0.62 V), the potential is scanned until a current density of 40 mA cm^{-2} is reached. Then, hydrogen evolved under

galvanostatic conditions at this current density for 1 to 10 minutes, followed by a potential sweep to a value at which the anodic current density approaches zero, but before the onset of oxidation of other coating components.

As illustrated in Figure 10a, the anodic region increases with longer hydrogen-evolution durations at the electrode surface. The total charge required for desorption of the absorbed hydrogen is shown in Figure 10b. It is demonstrated that after 10 minutes of electrolysis, the CoRe alloy approaches hydrogen saturation. For the coating containing 17.7 at.% Re, this value reaches 596 mA h, corresponding to $2.29 \cdot 10^{-4}$ mol(H)/g(alloy) or $2.51 \cdot 10^{-2}$ mol(H)/mol(alloy).

The potentiodynamic voltammograms also exhibit a cathodic current peak at about -1.0 V, the magnitude of which depends on the duration of electrode exposure at the cathodic current density. To clarify the nature of this peak, cyclic voltammograms were recorded as a function of the potential scan rate (Figure 11(a)). Prior to each measurement, hydrogen was evolved at a current density of 40 mA cm^{-2} for 10 minutes. The anodic portion of the voltammogram corresponds to the oxidation of absorbed hydrogen. The presence of a split peak may indicate the diffusion of hydrogen atoms from both near-surface and deeper layers of the coating. A cathodic peak in the polarization curve has been reported for palladium nanoparticles by Zalineeva *et al.* [43], who attribute it to hydrogen adsorption and electroabsorption.

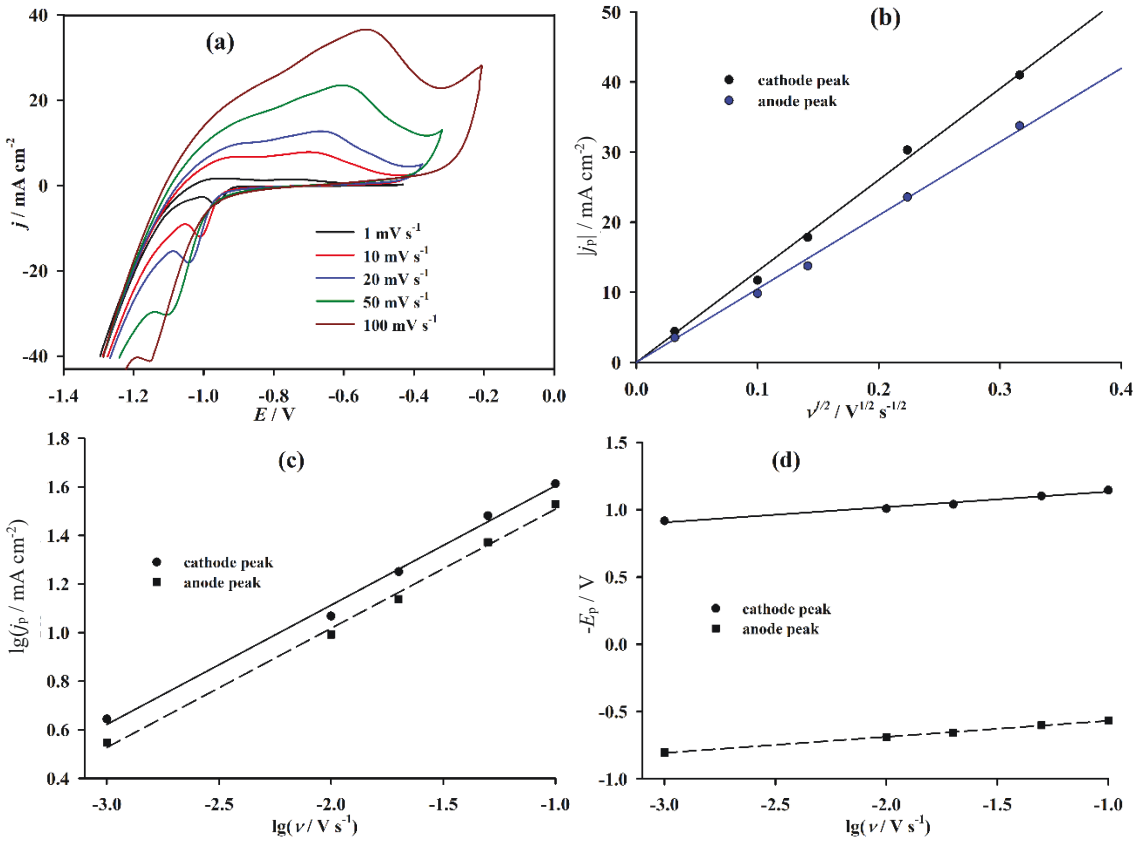

Figure 11. *(a) Cyclic voltammograms of hydrogen oxidation/reduction at different potential scan rates on CoRe coating containing 17.7 at.% Re, and dependence of: (b) anodic and cathodic peak current densities on square root of scan rate, and log of anodic and cathodic (c) peak current densities and (d) peak potential on log scan rate*

According to Figure 11b, in our experiment, both the anodic and cathodic peaks exhibit diffusion-controlled behaviour, as evidenced by linear j_p vs. $\nu^{1/2}$ plots that pass through the origin. The Semerano criterion, calculated from the slope of the log j_p *vs*. log ν plots in Figure 11(c), equals 0.5. The effective transfer coefficient (α'), determined from the dependence of E_p on log ν for both

anodic and cathodic processes shown in Figure 11(d), ranges from 0.48 to 0.52, *i.e*. approximately 0.5. These results contradict the hypothesis that the cathodic peak is adsorption-controlled and confirm that it is diffusion-controlled.

Since the cathodic process involves the addition of an electron to a species with diffusion limitations, that species cannot be protons from the bulk solution, given their high diffusion coefficient. The only protons exhibiting diffusion limitations are those located within the coating. Traditionally, electrochemical hydrogenation is associated with the insertion of atomic hydrogen into the interstitial sites of the metal crystal lattice [44].

The appearance of a cathodic peak on the voltammogram is sometimes attributed to the reduction of metal oxides formed when the cyclic voltammetry scan is extended far into the anodic region beyond the potential required to oxidize absorbed hydrogen. In the anodic region, the metal surface becomes oxidized, and upon reversing the scan toward cathodic potentials, a peak associated with oxide reduction may appear. However, in our experiment, the potential scan is limited to values more negative than the coating's open-circuit potential in the given solution.

Based on the slope of the j_p *vs.* $\nu^{1/2}$ dependence and according to Equation (4) for diffusion-controlled processes, the diffusion coefficients of hydrogen atoms involved in the anodic and cathodic processes were calculated using Equation (6):

$$i_p = 2.69\times10^5 n^{3/2} A D^{1/2} \nu^{1/2} C_H \quad (6)$$

where i_p / A is the peak current on the voltammogram; n is the number of electrons involved in the reaction; A / cm² is the electrode surface area; D / cm² s^{-1} is the diffusion coefficient and C_H / mol cm^{-3} is the hydrogen concentration. The hydrogen concentration is calculated based on the total charge passed (*i.e.* the area under the cathodic and anodic peaks in Figure 11a) and the volume of the coating, which is determined from the electrode weight gain and the alloy density, taking into account the metal content. The calculated diffusion coefficients are 1.5×10^{-14} cm² s^{-1} for the anodic peak and 10^{-12} cm² s^{-1} for the cathodic peak. This order of magnitude for D is consistent with findings reported by [45], which show that a low diffusion coefficient characterizes the β-hydride phase and increases by several orders of magnitude upon formation of the α-solid solution of hydrogen in the intermetallic. Similar diffusion behaviour of hydrogen has also been reported for metal hydride electrodes of AB_3-type [46] and AB_2-type systems [47] and is considered typical for hydride-forming alloys.

To obtain the dependencies shown in Figure 12, the alloy is subjected to hydrogen charging at a cathodic current density of 40 mA cm^{-2} for 0.5 to 10 minutes.

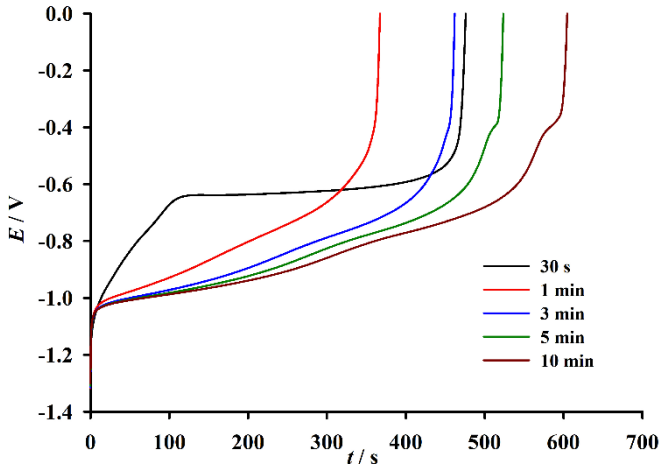

Figure 12. *Chronopotentiograms of hydrogen desorption at a constant anodic current density of 1.2 mA cm^{-2} for the CoRe alloy containing 17.7 at.% Re*

Figure 12 reveals the occurrence of two distinct processes: in the potential range from -1.1 to -0.65 V, the time required for the potential to change is proportional to the hydrogenation time. At -0.65 V for the first curve, and at -0.55 V for the fourth and fifth curves (5 and 10 min), a plateau in the chronopotentiogram is observed, where the potential remains near constant over time. This is followed by a sharp increase in potential until it reaches a steady-state value under the applied current density. The appearance of a potential plateau in the first curve may be associated with the decomposition of an intermetallic hydride formed during the electrodeposition process. The amount of charge required for hydride decomposition is approximately 0.12 mA h. Short-term hydrogen charging does not result in hydride formation; only at hydrogen-evolution durations of 5 to 10 minutes is hydride formation in the coating sufficient to produce the plateau in the chronopotentiogram. The plateau length increases with longer hydrogenation times, and the corresponding charge *Q* varies from 6.67·to 17.70·10^{-5} μA h.

The hydrogen absorption processes can be described as follows [48]: (a) hydrogen molecules are physically adsorbed on the surface of the particle; (b) hydrogen atoms are chemisorbed on the metal surface (*i.e*. chemisorption); (c) chemisorbed hydrogen atoms diffuse from the surface into the bulk (*i.e*. subsurface penetration); (d) metal hydride (MH) nucleates and grows when the hydrogen concentration exceeds the solid solubility limit.

As shown in Figure 13a, for alloys with different rhenium content, an increase in the anodic region, an increase in the cathodic peak magnitude, and a decrease in the hydrogen evolution overpotential are observed within the rhenium content range of 17.7 to 30.4 at.%. A further increase in the coating's rhenium content has the opposite effect. A similar trend is observed in Figure 8 for the steady-state HER voltammogram of freshly deposited coatings that were not subjected to additional hydrogen charging.

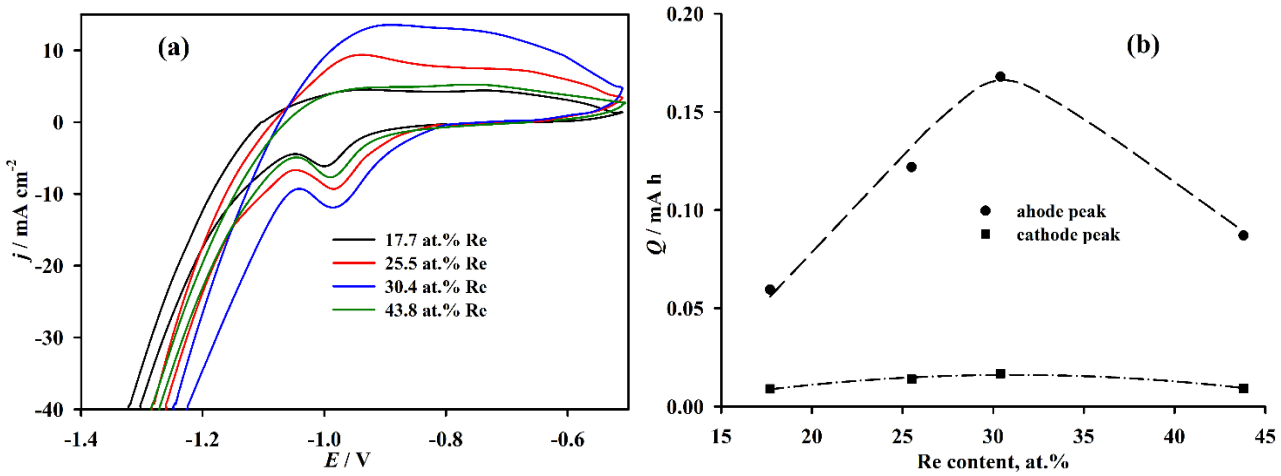

Figure 13. *(a) Cyclic voltammograms of hydrogen absorption/desorption and (b) the amount of charge consumed for hydrogen desorption on CoRe alloys with different rhenium content after 10 minutes of hydrogen charging. Scan rate is 10 mV* s^{-1}

The total charge required for desorption of absorbed hydrogen corresponds to the sum of the anodic and cathodic peak areas shown in Figure 13(b). Based on this charge and the mass of the coating, the hydrogen weight percentages are calculated to be 0.026, 0.00072, 0.056, and 0.030 wt.% H for alloys containing 17.7, 25.5, 30.4, and 43.8 at.% Re, respectively. Due to the high atomic weight of rhenium, these hydrogen concentrations may appear low in weight percent; however, when recalculated in atomic percent, it becomes evident that Co-Re alloys are capable of absorbing substantial amounts of hydrogen: 2.1, 6.1, 5.2, and 3.4 at.% H across the respective rhenium content range.

It is well known that intermetallic compounds are promising materials for hydrogen storage in the form of hydrides [49]. Alloys with Laves-phase crystal structures exhibit the highest hydrogen storage capacities [50]. Ideally, the atomic radius ratio of constituent elements for the formation of Laves phases is 1.225. For rhenium and cobalt, this ratio is 1.096, with the larger-radius atom occupying the A site and the smaller one the B site. Among the alloys obtained in this study, the one containing 30.4 at.% Re demonstrates the highest hydrogen storage capacity, corresponding to a Re:Co atomic ratio of 1:2. This composition creates favorable conditions for the formation of an AB_2-type intermetallic compound, specifically $ReCo_2$. Since cobalt can be electrodeposited individually from the pyrophosphate-ammonia electrolyte, whereas rhenium can only be deposited in conjunction with cobalt as part of an alloy, the decrease in hydrogen capacity when deviating from the 1:2 ratio may be attributed either to the dissolution of the formed intermetallic in the cobalt matrix (as in the alloy with 17.7 at.% Re), or to the properties of the solid solution formed by rhenium in cobalt.

Beyond the established mechanism of hydrogen evolution in alkaline media, Equations (7) to (9), the process may also involve additional stages related to the formation and decomposition of phases capable of absorbing hydrogen.

Volmer reaction $H_2O + \bar{e} \rightarrow H_{ads} + OH^-$ (7)

Heyrovsky reaction $H_2O + \bar{e} + H_{ads} \rightarrow H_2 + OH^-$ (8)

Tafel reaction $+ H_{ads} \rightarrow H_2$ (9)

These include the ε-CoRe solid solution, in which atomic hydrogen occupies interstitial sites in the expanded crystal lattice, as well as the intermetallic compound $ReCo_2$, Equations (10) to (13):

$\varepsilon\text{-CoRe} + xH_{ads} \rightarrow \varepsilon\text{-CoReH}_x$ (10)

$\varepsilon\text{-CoReHx} + H_{ads} \rightarrow \varepsilon\text{-CoReH}_{x-1} + H_2$ (11)

$ReCo_2 + xH_{ads} \rightarrow ReCo_2H_x$ (12)

$ReCo_2H_x + H_{ads} \rightarrow ReCo_2H_{x-1} + H_2$ (13)

The decrease in hydrogen overpotential on the hydrogenated coating may indicate that reactions (9) and (11) are more energetically favourable than electrochemical desorption and recombination processes.

Huang *et al*. [38] investigated hydrogen absorption during the electrodeposition of NiRe alloys. It was shown that the amount of cathodically absorbed hydrogen increases with increasing rhenium content in the coating and that the absorbed hydrogen exists in a stable hydride state. When the amount of adsorbed hydrogen exceeds its solubility in the stable hydride phase, cracking of the alloy deposit occurs. However, retaining hydrogen in the coating as a stable hydride enables crack-free deposits.

Under our experimental conditions, this suggests that for CoRe alloys, a rhenium content not exceeding 15 to 20 at.% is optimal for obtaining crack-free coatings, while a content of approximately 30 at.% Re is preferable for achieving high electrocatalytic activity and hydrogen absorption capability.

Despite existing guidelines from the U.S. Department of Energy (DOE), hydride materials derived from refractory metal alloys exhibit great potential for hydrogen storage, with capacities reaching up to 1.81 wt.% of adsorbed hydrogen [51]. Such materials may be particularly suitable for use in systems where the weight of the hydrogen tank is not a critical factor.

Conclusions

- CoRe alloy coatings with a rhenium content of 17.7 to 43.8 at.% and current efficiency up to 76 % are electrodeposited from a polyligand pyrophosphate-ammonia electrolyte, depending on the deposition current density and perrhenate ion concentration in the solution.

- The electrodeposition of the alloys proceeds under mixed diffusion-kinetic control with a preceding chemical dissociation stage of the $[Co(NH_3)_2(P_2O_7)]^{2-}$ polyligand complex. Simultaneous intensive hydrogen evolution leads to the formation of stressed deposits prone to cracking.
- During the codeposition of cobalt and rhenium, a solid solution of rhenium in hcp cobalt is primarily formed. The lattice parameters of this phase increase with increasing rhenium content. Additionally, the formation of an fcc cobalt-based solid solution is observed, and intermetallic compounds may also form.
- The highest electrocatalytic activity in the hydrogen evolution reaction is exhibited by the alloy containing 30.4 at.% Re. This composition also demonstrates the highest hydrogen absorption capacity. Hydrogen sorption studies reveal two distinct processes: the dissolution of atomic hydrogen into the alloy's expanded crystal lattice and the formation of intermetallic hydrides, with a total hydrogen uptake of up to 6 at.%.

Conflicts of interest: *The authors declare no conflict of interest.*

Acknowledgements: *This work was performed with the financial support of the National Academy of Sciences of Ukraine within the state budget theme «Finishing processing of materials in order to give them unique functional properties» 0123U100650.*

References

[1] A. M. R. Ramírez, S. Heidari, A. Vergara, M. V. Aguilera, P. Preuss, M. B. Camarada, A. Fischer, Rhenium-Based Electrocatalysts for Water Splitting, *ACS Materials Au* **3** (2023) 177-200. https://doi.org/10.1021/acsmaterialsau.2c00077

[2] P. Sabatier, Hydrogénations et déshydrogénations par catalyse, *European Journal of Inorganic Chemistry* **44** (1911) 1984-2001. https://doi.org/10.1002/CBER.19110440303 (in French)

[3] P. Yu, F. Wang, T. A. Shifa, X. Zhan, X. Lou, F. Xia, J. He, Earth abundant materials beyond transition metal dichalcogenides: A focus on electrocatalyzing hydrogen evolution reaction, *Nano Energy* **58** (2019) 244-276. https://doi.org/10.1016/j.nanoen.2019.01.017

[4] W. Sheng, M. Myint, J. G. Chen, Y. Yan, Correlating the hydrogen evolution reaction activity in alkaline electrolytes with the hydrogen binding energy on monometallic surfaces, *Energy & Environmental Science* **6** (2013) 1509-1512. https://doi.org/10.1039/C3EE00045A

[5] T. Jones, Rhenium plating, *Metal Finishing* **101** (2003) 86-96. https://doi.org/10.1016/S0026-0576(03)80439-7

[6] Huazhen Cao, Dagan Chai, Liankui Wu, Guoqu Zheng, Communication—A Mechanistic Study on Electrodeposition of Rhenium from Acidic Solution of Ammonium Perrhenate, *Journal of The Electrochemical Society* **164** (2017) D825-D827. https://doi.org/10.1149/2.0871713jes

[7] N. D. Ivanova, S. V. Ivanov, E. I. Boldyrev, Electrodeposition of rhenium coatings, *Functional Materials* **7** (2000) 350-352. https://functmaterials.org.ua/contents/7-2/35.htm

[8] N. Eliaz, E. Gileadi, *Induced codeposition of alloys of tungsten, molybdenum and rhenium with transition metals*, in *Modern Aspects of Electrochemistry*, C.G. Vayenas, R.E. White, M.E. Gamboa-Aldeco, Ed(s), Springer, New York, 2008, 191. https://doi.org/10.1007/978-0-387-49489-0_4

[9] W. M. Latimer, *Oxidation potentials 2nd ed.* Prentice Hall, New Jersey: Englewood Cliffs, 1952, p. 333. https://www.scirp.org/reference/referencespapers?referenceid=271066

[10] P. A. Nikolaychuk, The potential - pH diagram for rhenium, *Chemical Thermodynamics and Thermal Analysis* **7** (2022) 100068. https://doi.org/10.1016/j.ctta.2022.100068

[11] D. Mittendorf, G. A. West, New Processes to Produce Rhenium Metal Shapes, *Materials and Manufacturing Processes* **13** (1998) 749. https://doi.org/10.1080/10426919808935296

[12] A. R. Meyer, The Electrodeposition of Rhenium, *Transactions of the IMF* **46** (1968) 209-212. https://doi.org/10.1080/00202967.1968.11870073

[13] J. Chun, S. Jeon, K. Ra, I. Chun, The phase-shift method for determining Langmuir adsorption isotherms of over-potentially deposited hydrogen for the cathodic H_2 evolution reaction at poly-Re/aqueous electrolyte interfaces, *International Journal of Hydrogen Energy* **30** (2005) 485. https://doi.org/10.1016/j.ijhydene.2004.04.012
[14] J. O. Zerbino, A. M. Castro Luna, A Comparative Study of Electrochemical and Optical Properties of Rhenium Deposited on Gold and Platinum, *The Journal of the Brazilian Chemical Society* **13** (2002) 510. https://doi.org/10.1590/S0103-50532002000400016
[15] Yu. S. Yapontseva, T. V. Maltseva, V. S. Kublanovsky, O. A. Vyshnevskyi, Yu. N. Troshchenkov, Electrodeposition and properties of Co-Re alloys, *International Journal of Refractory Metals and Hard Materials* **96** (2021) 105469. https://doi.org/10.1016/j.ijrmhm.2021.105469
[16] A. Naor, N. Eliaz, E. Gileadi, Electrodeposition of Alloys of Rhenium with Iron-Group Metals from Aqueous Solutions, *Journal of The Electrochemical Society* **157** (2010) D422-D427. https://doi.org/10.1149/1.3327232
[17] Y. S. Yapontseva, V. S. Kublanovsky, T. V. Maltseva, Y. N. Troshchenkov, O. A. Vyshnevskyi, Electrodeposition, composition and properties of cobalt-rhenium alloys coatings, *Materials Advances* **4** (2023) 3662-3670. https://doi.org/10.1039/D3MA00309D
[18] O. O. Ostapets, Yu. S. Yapontseva, *Voltammetric Investigation of the Formation of Binary AgCo, CoRe and Ternary AgCoRe Alloys*, in *Modern aspects of electrochemistry. Collective monograph,* MPBP "Gordon", Kyiv, 2024, p. 210. https://doi.org/10.33609/elchimcongr.2024.09.1-210
[19] J. E. Castle*, Practical surface analysis by Auger and X-ray photoelectron spectroscopy,* D. Briggs and M. P. Seah (Editors), John Wiley and Sons Ltd, Chichester, 1983, p. 533. https://doi.org/10.1002/sia.740060611
[20] J. Heyrovsky, J. Kuta, *Principles of Polarography*, Academic Press, New York, NY, USA, 1965. https://api.pageplace.de/preview/DT0400.9781483264783_A23444968/preview-9781483264783_A23444968.pdf
[21] R. Guidelli, R. Compton, J. Feliu, E. Gileadi, J. Lipkowski, W. Schmickler, S. Trasatti Defining the transfer coefficient in electrochemistry: An assessment (IUPAC Technical Report), *Pure and Applied Chemistry* **86** (2014) 245-258. https://doi.org/10.1515/pac-2014-5026
[22] H. P. Myers, W. Sucksmith, The Spontaneous Magnetization of Cobalt, *Proceedings of the Royal Society of London. Series A, Mathematical and Physical Sciences* **207** (1951) 427-446. https://doi.org/10.1098/rspa.1951.0132
[23] S. Armyanov, Crystallographic Structure and Magnetic Properties of Electrodeposited Cobalt and Cobalt Alloys, *Electrochimica Acta* **45** (2000) 3323-3335. https://doi.org/10.1016/S0013-4686(00)00408-4
[24] X. Ma, Y. Ma, A. M. Nolan, J. Bai, W. Xu, Y.-Mo, H.-Chen, Understanding the Polymorphism of Cobalt Nanoparticles Formed in Electrodeposition - An *In Situ* XRD Study, *ACS Materials Letters* **5** (2023) 979-984. https://doi.org/10.1021/acsmaterialslett.2c00861
[25] ASTM PDF-01-077-7453 (hcp-Co), available online: https://icdd.com
[26] ASTM PDF-00-015-0806 (fcc-Co), available online: https://icdd.com
[27] O. M. Barabash, Y. N. Koval, *Crystal structure of metals and alloys,* Naukova Dumka, Kiev, 1986.
[28] A. Vicenzo, P.L. Cavallotti, Growth modes of electrodeposited cobalt, *Electrochimica Acta* **49** (2004) 4079-4089. https://doi.org/10.1016/j.electacta.2004.04.001
[29] J.-C. Crivello, A. Breidi, J.-M. Joubert, χ and σ Phases in Binary Rhenium-Transition Metal Systems: a Systematic First-Principles Investigation, *Inorganic Chemistry* **52** (2013) 3674-3686. https://doi.org/10.1021/ic302142w

[30] O. Levy, M. Jahnátek, R. V. Chepulskii, G. L. W. Hart, S. Curtarolo, Ordered Structures in Rhenium Binary Alloys from First-Principles Calculations, *Journal of the American Chemical Society* **133** (2011) 158-163. https://doi.org/10.1021/ja1091672
[31] C. M. F. Rae, R. C. Reed, The precipitation of topologically close-packed phases in rhenium-containing superalloys, *Acta Materialia* **49** (2001) 4113-4125. https://doi.org/10.1016/S1359-6454(01)00265-8
[32] W. Köster, E. Horn, Zustandsbild und Gitterkonstanten der Legierungen des Kobalts mit Rhenium, Ruthenium, Osmium, Rhodium und Iridium, *International Journal of Materials Research* **43** (1952) 444-449. https://doi.org/10.1515/ijmr-1952-431206 (In German).
[33] A. Cimino, B. A. De Angelis, D. Gazzoli, M. Z. Valigi, Photoelectron Spectroscopy (XPS) and Thermogravimetry (TG) of Pure and Supported Rhenium Oxides. 1. Pure Rhenium Compounds, *Zeitschrift für anorganische und allgemeine Chemie (ZAAC)* **460** (1980) 86-98. https://doi.org/10.1002/zaac.19804600109
[34] O. Berkh, L. Burstein, A. Gladkikh, N. Eliaz, E. Gileadi, Characterization of Re-Ni Films after the Initial Stages of Electrodeposition, *Journal of The Electrochemical Society* **163** (2016) D295-D299. https://doi.org/10.1149/2.0631607jes
[35] C. J. Powell, Recommended Auger parameters for 42 elemental solids, *Journal of Electron Spectroscopy and Related Phenomena* **185** (2012) 1-3. https://doi.org/10.1016/j.elspec.2011.12.001
[36] A. B. Mandale, S. Badrinarayanan, S. K. Date, A. P. B. Sinha, Photoelectron-spectroscopic study of nickel, manganese and cobalt selenides, *Journal of Electron Spectroscopy and Related Phenomena* **33** (1984) 61-72. https://doi.org/10.1016/0368-2048(84)80006-7
[37] B. A. Rosen, E. Gileadi, N. Eliaz, Electrodeposited Re-promoted Ni foams as a catalyst for the dry reforming of methane, *Catalysis Communications* **76** (2016) 23-28. https://doi.org/10.1016/j.catcom.2015.12.014
[38] C.-H. Huang, J.-R. Jan, W.-Y. Shu, H.-M. Wu, The sulfur-enhanced effect of absorbing hydrogen in electroformed nickel-rhenium alloy, *Materials Chemistry and Physics* **70** (2001) 168-174. https://doi.org/10.1016/S0254-0584(00)00494-6
[39] Yu. S. Yapontseva, V. N. Zaichenko, V. S. Kublanovsky, O. Yu. Gorobets, Yu. M. Troshchenkov, O. A. Vyshnevskyi, Effect of a Constant Magnetic Field on Electrodeposition of CoMo, CoRe, and CoMoRe Alloys from a Citrate Electrolyte, *Surface Engineering and Applied Electrochemistry* **59** (2023) 412-421. https://doi.org/10.3103/S106837552304018X
[40] Yu. S. Yapontseva, T. V. Maltseva, V. S. Kublanovsky, Electrocatalytic and Corrosion Properties of CoWRe Alloys Electrodeposited from a Citrate-Pyrophosphate Electrolyte, *Metallophysics and Advanced Technologies / Metallofizika i Noveishie Tekhnologii* **46** (2024) 491-505. https://doi.org/10.15407/mfint.46.05.0491
[41] J. N. Han, S. Pyun, T. H. Yang Roles of Thiourea as an Inhibitor in Hydrogen Absorption into Palladium Electrode, *Journal of The Electrochemical Society* **44** (1997) 4266. https://doi.org/10.1149/1.1838176
[42] D.R. Gabe, The role of hydrogen in metal electrodeposition processes. *Journal of Applied Electrochemistry* **27** (1997) 908-915. https://doi.org/10.1023/A:1018497401365
[43] A. Zalineeva, S. Baranton, C. Coutanceau, G. Jerkiewicz, Electrochemical Behavior of Unsupported Shaped Palladium Nanoparticles, *Langmuir* **31** (2015) 1605-1609. https://doi.org/10.1021/la5025229
[44] K. Komander, T. Tran, J. Saha, M. V. Moro, G. K. Pálsson, M. Wolff, D. Primetzhofer, Interstitial Hydrogen in Fe/V Superstructures: Lattice Site Location and Thermal Vibration, *Physical Review Letters* **127** (2021) 136102. https://doi.org/10.1103/PhysRevLett.127.136102

[45] B. S. Haran, B. N. Popov, R. E. White, Determination of the hydrogen diffusion coefficient in metal hydrides by impedance spectroscopy, *Journal of Power Sources* **75** (1998) 56-63. https://doi.org/10.1016/S0378-7753(98)00092-5

[46] A. A. Volodin, C. Wan, R. V. Denys, G. A. Tsirlina, B. P. Tarasov, M. Fichtner, U. Ulmer, Y. Yu, C. C. Nwakwuo, V. A. Yartys, Phase-structural transformations in a metal hydride battery anode $La_{1.5}Nd_{0.5}MgNi_9$ alloy and its electrochemical performance, *International Journal of Hydrogen Energy* **41** (2016) 9954-9967. https://doi.org/10.1016/j.ijhydene.2016.01.089

[47] I. D. Wijayanti, R. Denys, Suwarno, A. A. Volodin, M.V. Lototskyy, M. N. Guzik, J. Nei, K. Young, H. J. Roven, V. Yartys, Hydrides of Laves type Ti-Zr alloys with enhanced H storage capacity as advanced metal hydride battery anodes, *Journal of Alloys and Compounds* **793** (2019) 564-575. https://doi.org/10.1016/j.jallcom.2020.154354

[48] Q. Li, X. Lin, Q. Luo, Y. Chen, J. Wang, B. Jiang, F. Pan, Kinetics of the hydrogen absorption and desorption processes of hydrogen storage alloys: A review, *International Journal of Minerals, Metallurgy and Materials* **29** (2022) 32-48. https://doi.org/10.1007/s12613-021-2337-8

[49] R. Ströbel, J. Garche, P. T. Moseley, L. Jörissen, G. Wolf, Hydrogen storage by carbon materials, *Journal of Power Sources* **159** (2006) 781-801. https://doi.org/10.1016/j.jpowsour.2006.03.047

[50] V. A. Yartys, M. V. Lototskyy, Laves type intermetallic compounds as hydrogen storage materials: A review, *The Journal of Alloys and Compounds* **916** (2022) 165219. https://doi.org/10.1016/j.jallcom.2022.165219

[51] M. S. Xaba, Additively manufactured high-entropy alloys for hydrogen storage: Predictions, *Heliyon* **10** (2024) e32715. https://doi.org/10.1016/j.heliyon.2024.e32715